Journal of Global Positioning Systems (2026)
Vol. 22, Issue 1: 75-89
DOI:10.5081/jgps.22.1.75

Journal of Global Positioning Systems
2026
© CPGPS

A Gradient-Aware Undersampled Ionospheric Threat Model with Multi Metrics for BDSBAS

Hui Ren[1], Zhengzhen Jin[1], Tong Liu[2], Fangxin Hu[3,4], and Yiping Jiang[1] ✉

1 Department of Aeronautical and Aviation Engineering, The Hong Kong Polytechnic University (HKPolyU), China
2 Department of Land Surveying and Geo-Informatics, HKPolyU, China
3 School of Geodesy and Geomatics, Wuhan University, Wuhan, China
4 School of Aerospace, Harbin Institute of Technology (Shenzhen), Shenzhen, China

✉**:** yiping.jiang@polyu.edu.hk

ABSTRACT: Satellite-based augmentation systems (SBAS) broadcast grid ionospheric vertical delays (GIVDs) together with their integrity bounds, known as grid ionospheric vertical errors (GIVEs), to support accurate and integrity-assured positioning. In regions such as China, characterized by wide latitude coverage and highly dynamic ionospheric behaviour, geometric descriptors of IPP distribution alone are insufficient to capture local ionospheric variability. This limitation prevents conventional undersampled threat models from distinguishing between benign and severe conditions, leading to excessive GIVE inflation and reduced availability. This paper proposes a gradient-aware undersampled ionospheric threat model for BeiDou satellite-based augmentation system (BDSBAS) in China, referred to as the RRG-3D framework. The method extends the conventional geometry-based model by introducing a statistical ionospheric gradient metric, P90G, defined as the 90th percentile of pairwise gradients to characterize local variability. By integrating geometric descriptors with physical ionospheric variability, the undersampled threat model is reformulated from a 2D lookup table into a coupled geometry-gradient 3D representation. The model is evaluated using a complete storm event in May 2024 over 117 BDSBAS IGPs. Results show that RRG-3D effectively reduces undersampled threats and alleviates the excessive conservatism of GIVE, while strictly preserving the integrity requirement, thereby improving BDSBAS availability. From the integrity perspective, The IGP-averaged undersampled threat is reduced by 50.94%, and total uncertainty by 20.74%. Improvements are more pronounced at central IGPs and high-latitude regions, where gradients are relatively mild, while gains are limited in low-latitude regions dominated by strong gradients. From the availability perspective, the proposed model achieves consistent improvements for both APV-I and LPV-200 services. At the 99% availability level, coverage increases by 24.25% and 61.48%, respectively, with larger gains under stricter availability requirements. This work demonstrates that incorporating ionospheric gradient information enables a more physically meaningful characterization of undersampled threats, reducing unnecessary conservatism while maintaining integrity, and ultimately enhancing SBAS availability under complex ionospheric conditions.

KEYWORDS: BDSBAS, Ionospheric under-sampled threat model, Integrity, Availability, Gradient

I. Introduction

Signals transmitted by Global Navigation Satellite Systems (GNSS) are significantly affected by ionospheric propagation delays, whose complex variability introduces major positioning errors, especially for safety critical applications such as precision approaches. To meet stringent requirements on integrity and availability, Satellite-Based Augmentation Systems (SBAS) provide ionospheric corrections together with associated uncertainty bounds that are used to compute user protection levels (Jiang and Wang 2016; Ren et al. 2024). However, due to the discrete and limited distribution of ground monitoring stations, ionospheric observations are inherently undersampled, leading to unmodeled errors beyond measurement noise and model mismatch. To ensure safe operation under all conditions, these errors must be conservatively bounded through the inflation of uncertainty, making the construction of an effective ionospheric undersampled threat model essential for SBAS performance.

Current SBAS systems adopt grid-based ionospheric correction schemes, in which grid ionospheric vertical delays (GIVDs) are estimated at predefined ionospheric grid points (IGPs) using observations from nearby ionospheric pierce points (IPPs) through interpolation methods such as kriging in Wide Area Augmentation System (WAAS) or triangular interpolation in European Geostationary Navigation Overlay Service (EGNOS) (El-Arini et al. 1994; Prasad and Sarma 2007; Alleau et al. 2013; Trilles et al. 2015). To ensure safety-of-life integrity, SBAS further broadcasts at each IGP a conservative uncertainty bound known as the grid ionospheric vertical error (GIVE), typically constructed as a high-confidence overbound (e.g., 99.9%) of the residual ionospheric delay (Blanch et al. 2018). This integrity information is propagated to the user and used to compute horizontal and vertical protection levels (HPL/VPL), which are compared against alert limits to determine service availability. Due to the discrete and limited distribution of ground monitoring stations, ionospheric observations are inherently undersampled, and estimation based on surrounding IPPs may fail to capture localized ionospheric irregularities, especially under disturbed conditions. As a result, the associated estimation errors are not fully reflected in the formal uncertainty posing potential integrity risks. To address this issue, SBAS employs ionospheric threat models that relate IPP distribution characteristics to worst-case estimation errors and inflate GIVE accordingly. Nevertheless, such inflation may lead to overly conservative protection levels, thereby reducing availability.

The construction of an undersampled ionospheric threat model fundamentally depends on how the discrete IPPs distribution is abstracted into representative metrics, because the model is ultimately established as a mapping from IPPs distribution characteristics to the maximum estimation error under historical worst-case conditions (Sparks et al. 2011). In the classical WAAS framework, this problem was formulated as determining how large an ionospheric irregularity can be in an unobserved region when the chi square detector does not trigger, and the resulting threat model was therefore explicitly coupled to a set of metrics describing IPPs distribution (Blanch et al. 2002). Following this idea, the conventional two metric model based on fitting radius (R_{fit}) and relative centroid metric (RCM) has become the foundation of operational undersampled threat modelling, and a variety of geometry-based extensions have since been proposed to improve the description of IPP sampling patterns. These metrics can generally be divided into distance based, angle based, and coverage based categories, including RCMX (Pandya et al. 2007), double RCM or related variants (Junjie et al. 2018), maximum separation angle MSA (Sakai et al. 2008), empty pie shape EPS (Bang et al. 2013), norm-based angular metric (NAM) (Bang and Lee 2023) and relative coverage metric RCOV (Zhang et al. 2020). More recently, several studies have further extended the conventional 2D threat space by introducing an additional geometry-related metric, such as NAM or minimum separation distance (Zhang et al. 2017; Bang and Lee 2023; Wang et al. 2025). Although these approaches increase the dimensionality of the threat model, the additional metric still characterizes the spatial sampling configuration of IPPs rather than the physical state of the ionosphere

However, all these metrics remain descriptors of the monitoring geometry and do not explicitly characterize the physical variability of the ionosphere. implicitly assuming that similar IPP configurations correspond to similar ionospheric threat levels. This assumption is inherently limited, because multiple WAAS studies have shown that the real integrity risk arises not from geometry itself but from ionospheric irregularities and gradients that are insufficiently sampled by the monitoring network (Altshuler et al. 2001; Datta-Barua 2004). In particular, the blob and wall analyses demonstrated that severe residuals could develop rapidly outside apparently well sampled regions, meaning that similar geometric descriptors may correspond to very different physical threat levels (Blanch et al. 2002). This mismatch is especially important because geometry-based metrics cannot distinguish whether a given sampling pattern is associated with a threatening irregularity or with a relatively smooth ionospheric field. As a result, conventional models may underestimate the risk in regions affected by strong local gradients, while also producing unnecessarily conservative bounds in regions where gradients are mild.

This limitation is particularly relevant to the BDSBAS service region. Previous studies have shown that ionospheric gradients are generally stronger and more recurrent in low-latitude environments than in mid-latitude regions (Wang et al. 2017; Marini-Pereira et al. 2021). Furthermore, ionospheric gradient characteristics exhibit considerable regional variability. Compared with the nominal CONUS threat model, substantially larger gradient levels have been reported in several Asia-Pacific and low-latitude regions, including Japan, Brazil, Hong Kong, and Vietnam (Lee et al. 2015; Saito and Yoshihara 2017; Li and Jiang 2023; Saito et al. 2025), suggesting that gradient behaviour cannot be adequately represented by a universal parameter transferred between different SBAS service regions. This regional dependence further motivates the explicit incorporation of gradient information into BDSBAS threat modelling. More generally, the key limitation is that geometry-based metrics describe only the sampling configuration of IPPs and do not explicitly quantify the physical variability of the ionosphere within the sampled region. This motivates the incorporation of gradient information as an additional threat descriptor.

Conventional SBAS undersampled threat models rely only on spatial geometry descriptors and therefore cannot fully distinguish geometrically similar but physically different ionospheric scenarios. This limitation may lead to insufficient characterization of local ionospheric variability and, more importantly, to unnecessarily conservative GIVE inflation in regions where the actual gradient level is mild. To address this issue, this paper proposes a gradient-aware undersampled ionospheric threat model with multiple metrics for BDSBAS. Building on the conventional RR-2D framework, the proposed RRG-3D model introduces an additional gradient descriptor, P90G, to explicitly capture local ionospheric variability and extend the threat model from a purely geometry-based representation to a coupled geometry-gradient formulation. Section II introduces the GIVD estimation method, defines the proposed gradient metric P90G, and presents the construction procedure of the RRG-3D threat model. Section III evaluates the resulting integrity and availability performance over the BDSBAS China region and compares the proposed model with the conventional RR-2D framework. Finally, the main conclusions and implications of this work are summarized in Section IV.

II. Methodology

A. Universal Kriging for Ionospheric Delay Estimation

Universal Kriging (UnK), widely adopted in SBAS ionospheric modelling, is a geostatistical interpolation method that provides a minimum-variance, unbiased estimate of ionospheric delay by explicitly accounting for both large-scale spatial trends and small-scale stochastic variability. Compared with simpler approaches such as planar fitting, which assume a deterministic planar structure, UnK more accurately captures the irregular and spatially correlated behaviour of the ionosphere. In the UnK framework, the vertical ionospheric delay is modelled as a realization of a regression model consisting of deterministic spatial trend components and a stochastic residual process, as shown in Eq(1). Given a set of observed vertical ionospheric delays $I_v(s_i)$ at surrounding sampling locations (s_i), the delay at a target location (s_0) is estimated as a weighted linear combination of these observations in Eq(2).

$$I_v(\hat{x}_i^{(east)}, \hat{x}_i^{(north)}, t_i) = a_0 + a_1\hat{x}_i^{(east)} + a_2\hat{x}_i^{(north)} + r_i \quad (1)$$

where, a_0 represents the vertical delay estimation of the target point, $[a_1, a_2]$ denotes the spatial variation coefficients along the East and North direction in ENU system, $\hat{x}_i^{east}$ and $\hat{x}_i^{north}$are the distance between the observation and the target point along two directions, r_i is the random field indicating the small irregularities superimposed on the trend.

$$\hat{I}_v(s_0) = w^T I_{IPP} = \sum_{i=1}^{N} \omega_i I_v(s_i) \quad (2)$$

where ω_i is the weight of i^{th} sampling data, s_0 and s_i are location information of the point to be estimated and sampling point.

A key component of the Kriging method is the semi-variogram, which characterizes the spatial correlation structure of ionospheric delays. It reflects the fundamental property that nearby ionospheric pierce points exhibit stronger similarity, while correlation decreases with increasing distance. The semi-variogram is defined as the variance of the difference between ionospheric delays at two locations:

$$\gamma(d_{ij}) = \frac{1}{2}E[(I_V(s_i) - I_V(s_j))^2] \quad (3)$$

where d_{ij} denotes the separating spatial distance between IPP pairs.

The estimation satisfies the unbiasedness condition by constraining the sum weights to 1, ensuring zero expected prediction error. Meanwhile, optimality is achieved by minimizing the estimation variance in Eq(4) under this constraint, leading to a system of equations that can be solved using Lagrange multipliers. Although Eq. (4) is expressed in the semi-variogram form, the subsequent matrix formulation is equivalently written in terms of the covariance function, where the semi-variogram and covariance at the same separation distance h satisfy: $\gamma(h)=C(0)-C(h)$. Therefore, the weight solution vector Λ in Eq(5) is determined by both the spatial configuration of sampling points and their statistical dependence.

$$\min E[\hat{I}_v(s_0)-I_v(s_0)]^2=\min(2\sum_{i=1}^{N}\omega_i\gamma_{i0}-\sum_{i=1}^{N}\sum_{j=1}^{N}\omega_i\omega_j\gamma_{ij}) \quad (4)$$

$$\Lambda=[W-WG(G^TWG)^{-1}G^TW]c+WG(G^TWG)^{-1}s \quad (5)$$

where, the subscripts i and j denote the indices of the surrounding sampling IPPs, consistent with Eq. (2). $W = C^{-1}$ represents the weighting matrix. $C = Cov(r_{IPP}, r_{IPP}^T)$ is the covariance matrix of the ionospheric residuals between sampling IPPs. $c=Cov(r_{IPP}, r_0)$ is the covariance vector between IPPs and the target point. s is the constraint vector $[1\ 0\ 0\ 0]^T$. $G=\begin{bmatrix}1 & x_1\hat{e} & x_1\hat{n}\\ \dots & \dots & \dots\\ 1 & x_N\hat{e} & x_N\hat{n}\end{bmatrix}$ represents the observation trend matrix, $\hat{e}$and $\hat{n}$ denote the unit basis vectors along the east and north directions in the local ENU coordinate system.

After detrending ionospheric delays by planar fitting, many well-established theoretical variogram models can be used to fit experimental variograms, including the exponential, Gaussian, and Matérn models. In this study, a Gaussian variogram model in Eq(6) is adopted, with parameters configured according to Liu (Liu et al. 2017) for the China region.

$$\hat{\gamma}(d)=\begin{cases}0 & if\ d=0\\ C_0+(\sigma^2-C_0)(1-e^{-\frac{d^2}{h^2}}) & if\ d>0\end{cases} \quad (6)$$

where, C_0 is the nugget effect, representing the magnitude of the intercept and accounting for small-scale variability or measurement noise, with $C_0 = 0.45^2$. σ^2 represents the sill, set to 1.25^2. h is range, set as 8000 km. d is the separating distance.

Following WAAS approach, an IPP searching algorithm is employed to estimate unknown ionospheric delays using nearby IPPs. The candidate IPPs are selected based on four key parameters: minimum search radius (R_{min}), maximum search radius (R_{max}), number of target points (N_{target}) and minimum points (N_{min}), detailed in the relevant reference (Sparks et al. 2011). In this study, all parameter settings are kept fully consistent with the reference, with R_{min} =800 km, R_{max} = 2100 km, N_{min} = 10, N_{target} = 30.

B. Undersampled Threat Model Construction

In SBAS, GIVD provides ionospheric corrections at each IGP, while GIVE serves as a safety critical bound on the associated uncertainty. Conventional undersampled threat models primarily rely on the spatial distribution of IPPs and implicitly assume that irregular IPP geometry is the dominant source of unmodeled ionospheric error. However, this assumption does not fully reflect the intrinsic spatial variability of the ionosphere. In practice, even when IPPs are well distributed, strong local ionospheric gradients, especially under disturbed conditions or in low latitude regions, can introduce significant delay differences that are not adequately captured by geometry-based metrics alone. As a result, existing models may underestimate the true threat in regions with sharp gradients or overestimate the uncertainty in relatively smooth areas. This limitation motivates the introduction of ionospheric gradient information as an additional parameter in the undersampled threat model. By explicitly incorporating the spatial rate of change of ionospheric delay, the proposed approach enables a more physically meaningful characterization of ionospheric irregularities, complementing the conventional geometry-based indicators and leading to a more balanced and accurate estimation of undersampled threats.

To mitigate the risks arising from undersampled ionospheric conditions, SBAS introduces ionospheric threat models that inflate GIVE values according to the spatial configuration of surrounding IPPs. The primary purpose of these models is to establish a mapping between IPP distribution characteristics and the maximum estimation errors observed under historical worst-case scenarios. This concept was originally developed in WAAS through the classical two parameter framework based on R_{fit} and RCM, which continues to serve as the basis for operational undersampled threat modelling.

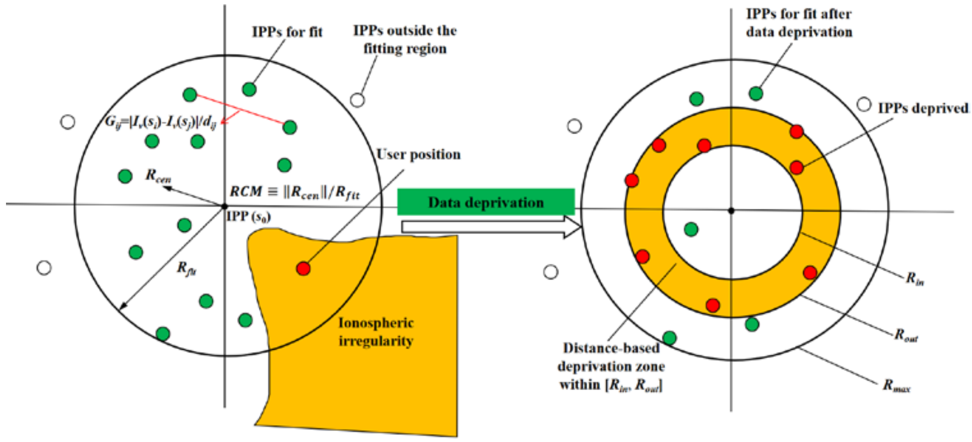

Fig. 1. Geometry metrics and P90 gradient description and data deprivation scheme for RRG-3D model

The undersampled threat, denoted as $\sigma_{undersampled}$, is typically defined as the standard deviation of a Gaussian distribution that captures both the formal estimation error and the residual error. After incorporating the undersampled threat, the resulting GIVE is required to conservatively bound the true ionospheric estimation error, thereby satisfying the following condition:

$$\left|I_k-\hat{I}_k\right|^2 = K^2_{undersampled}[\tilde{\sigma}_k^2+\sigma^2_{undersampled,k}] \tag{7}$$

$$\tilde{\sigma}_k^2 = R^2_{irreg}(\Lambda^T C\Lambda-2\Lambda^T c+\sigma^2) \tag{8}$$

where, I_k and $\hat{I}_k$ denote the observation and estimation of the vertical delay, respectively. $\tilde{\sigma}_k^2$ is the inflated formal kriging estimation variance. $R^2_{irreg}=\chi^2_{1-P_{fa}}/\chi^2_{P_{md}}$ is the inflation factor as a function of degree of freedom $\bar{N}$ based on the chi-square distribution. P_{md} is the missing detection probability, set as 10^{-3}. C is the covariance matrix among IPPs. c is the covariance vector between IPPs and the target point. σ^2 denotes the sill of variogram model. $K_{undersampled}$ is set to 5.33 corresponding to a confidence level 10^{-7} of integrity risk.

Conventional SBAS ionospheric undersampled threat models are constructed based on a two metric lookup table composed of R_{fit} and RCM, which is consistent with GIVD estimation using UnK. This RR-2D framework has been widely adopted in operational SBAS implementations and serves as the baseline reference in this study. However, as illustrated in Fig. 1, the conventional formulation characterizes IPP information only through spatial geometry and does not explicitly account for the spatial variability of ionospheric delays. In practice, even when two IPP configurations share similar geometric characteristics, their corresponding estimation risks may differ substantially if the surrounding ionosphere exhibits different levels of local gradient activity. To address this limitation, an additional gradient related metric, denoted as P90G, is introduced to complement the geometry-based description of undersampled conditions. For a target point s_0, P90G is defined as the 90th percentile of pairwise ionospheric gradients within the associated neighbouring IPP set $\Omega(s_0)$.

$$P90G(s_0)=Q_{0.9}\left\{\frac{\left|I_v(s_i)-I_v(s_j)\right|}{d_{ij}}\middle|(s_i,s_j)\in\Omega(s_0)\right\} \tag{9}$$

Unlike the additional metrics adopted in existing three-dimensional threat models, which quantify different aspects of IPP spatial distribution, P90G directly characterizes the local gradient level of the monitored ionosphere and therefore provides complementary physical information beyond the sampling geometry.

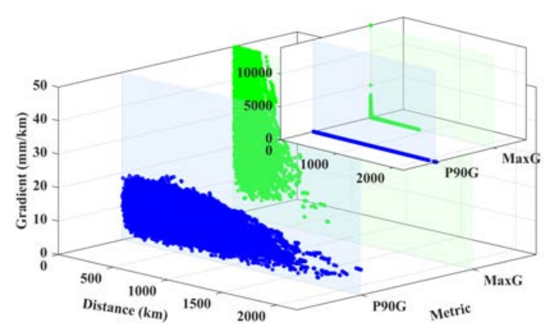

Fig. 2. Comparison of P90G and MaxG distributions for undersampled events during the six storm days.

To further illustrate the rationale for selecting P90G, Fig. 2 compares the distributions of P90G and the maximum gradient (MaxG) computed from all undersampled events during the six storm days. It can be observed that P90G exhibits a relatively stable distribution over a wide range of IPP separations, with values remaining below 22.4 mm/km. In contrast, MaxG contains a large number of values exceeding 50 mm/km, and in extreme cases can exceed 10000 mm/km. These large MaxG values are mostly concentrated at short IPP separations, typically below 500 km, indicating that MaxG is highly sensitive to short-baseline observational effects. By using the 90th percentile instead of the maximum value, P90G suppresses these isolated or short-baseline extremes while preserving the dominant gradient characteristics of the surrounding IPP set, making it a more robust descriptor.

In this study, a variable width annular data deprivation scheme is adopted to simulate a wide range of undersampled events, forming the basis for subsequent threat model construction. For each target IPP simulated as an IGP, nearby IPPs are first selected using the same IPP searching algorithm as in GIVD estimation, from which R_{fit} is determined. Then, IPPs located within an annular deprivation region $[R_{in}, R_{in}+R_w]$ are artificially removed, and the ionospheric delay at the target point is re estimated using the remaining observations. The inner radius R_{in} increases from 0 to R_{fit}-R_w in steps of 200 km. To generate a sufficiently rich set of threat events, the annulus width R_w is varied from 0.1 R_{fit} to 0.9 R_{fit} with a step size of 0.2 R_{fit}. For each valid deprivation case, the threat metrics $\{R_{fit}$, RCM, P90G$\}$ are computed, and the corresponding undersampled threat is derived from the estimation residual and formal error after statistical screening. In this way, the raw undersampled threat model is reformulated from the conventional 2D tabulation into a 3D tabulation parameterized by two geometry metrics and the statistical gradient metric.

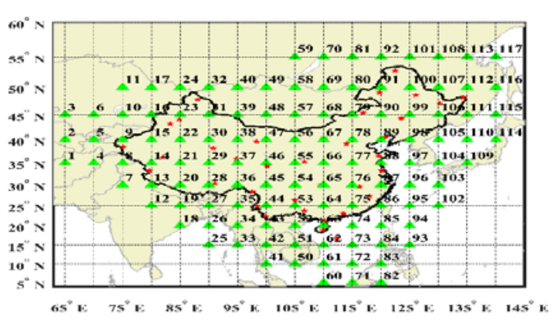

Fig. 3. Distribution of 36 monitor stations (red stars) and 117 BDSBAS IGPs (green triangles) with ID numbers

$$\sigma^{raw}_{undersampled}(R^i_{fit}, RCM^j, P90G^m) = \max_{over\ k,\, R_{in}, R_w}\left(\sqrt{\frac{(I_k-\tilde{I}_k)^2}{K^2_{undersampled}} - \tilde{\sigma}_k^2}\right) \quad (10)$$

After the threat model construction, the integrity bound GIVE can be calculated as the 99.9% confidence bound of total uncertainty:

$$GIVE = \kappa_{99.9\%}\sigma_{GIVE} = 3.29\sigma_{GIVE} \quad (11)$$

$$\sigma_{GIVE} = \sqrt{\tilde{\sigma}^2_{IGP} + \sigma^2_{undersampled}} \quad (12)$$

where, σ_{GIVE} represents the total uncertainty of GIVD estimation taking account of both inflated formal estimation error and the undersampled threat. $\kappa_{99.9\%}$ is the quantile of 99.9% confidence interval for Gaussian distribution.

C. Data Collection

To support the development and evaluation of a gradient-aware undersampled ionospheric threat model for BDSBAS, ionospheric delay observations were collected from a regional GNSS reference network configured to represent the operational characteristics of BDSBAS. As illustrated in Fig. 3, a total of 36 stations from the Crustal Movement Observation Network of China (CMONOC) were selected. The spatial distribution of these stations is comparable to that of the BDSBAS ground monitoring network, ensuring that the derived ionospheric behaviour and subsequent undersampled threat modelling are representative of real-world BDSBAS applications over the China region. Owing to confidentiality restrictions associated with CMONOC data, the station locations shown in Fig. 2 have been intentionally obfuscated using Gaussian perturbations with small positional drifts. 117 ionospheric grid points (IGPs), defined according to the BDSBAS service grid, are also shown in Fig. 3. These IGPs serve as evaluation nodes for ionospheric delay estimation and threat assessment.

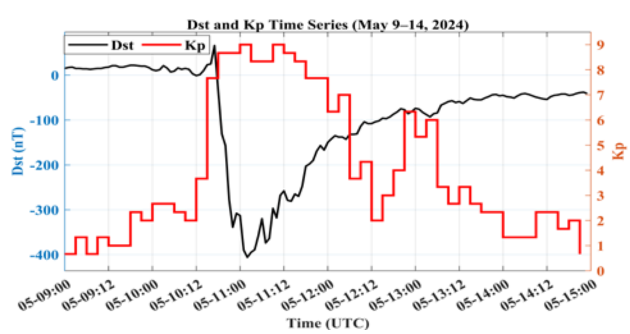

Fig. 4. Temporal variations of geomagnetic activity metrics (Kp and Dst) in the studied period

The observation data were sampled at 30-second intervals. Ionospheric vertical delays were derived from dual-frequency GNSS measurements using an improved "simple truth" approach, in which pseudo-range and carrier phase observations are combined to enhance estimation accuracy. Standard preprocessing steps were applied, including cycle slip detection, outlier removal, arc segmentation and merging, and carrier-phase levelling to pseudo-range observations, ensuring reliable ionospheric delay estimates for subsequent analysis. To capture worst-case ionospheric conditions for undersampled threat modelling and to evaluate integrity performance under extreme scenarios, a severe geomagnetic storm event from May 9 to May 14, 2024, was selected. The corresponding Dst and Kp time series are shown in Fig. 4. As indicated in the figure, geomagnetic conditions were relatively quiet on May 9. Around 12:00 UTC on May 10, the Dst index dropped rapidly while the Kp index increased significantly, indicating the onset of a strong geomagnetic disturbance. The storm reached its peak intensity on May 11, with Dst decreasing below -400 nT and Kp reaching 9, corresponding to an extreme ionospheric disturbance scenario. After May 12, geomagnetic activity gradually weakened and returned to relatively quiet conditions. This event provides a representative dataset for evaluating the robustness of the proposed geometry–gradient coupled undersampled ionospheric threat model under severe space weather conditions.

III. Results

This section evaluates the performance of the proposed gradient-aware undersampled ionospheric threat model using GIVE results, integrity assessment, and availability simulations for BDSBAS in the China region. For comparison, a conventional geometry-driven undersampled threat model based on two-metric indicators is adopted as the baseline. By comparing the two approaches, the effectiveness of incorporating ionospheric gradient information is demonstrated in terms of reducing excessive conservatism while maintaining integrity and improving system availability, in order to demonstrate the effectiveness of incorporating gradient information into undersampled threat modelling.

A. Gradient Expanded Threat Model

Conventional SBAS ionospheric undersampled threat models are typically constructed within a two-metric lookup table defined by R_{fit} and RCM, where the threat representation is primarily driven by spatial sampling geometry. This geometry-based formulation has been widely adopted in operational SBAS systems and serves as the baseline approach in this study. In contrast, the proposed model extends this framework by explicitly incorporating ionospheric gradient information, resulting in a coupled geometry-gradient three-dimensional undersampled threat model. By augmenting the conventional geometric descriptors with a physical characterization of ionospheric variability, the proposed approach aims to provide a more representative description of undersampled ionospheric threats. As mentioned before, a constant universal kriging model is applied to estimate ionospheric delays.

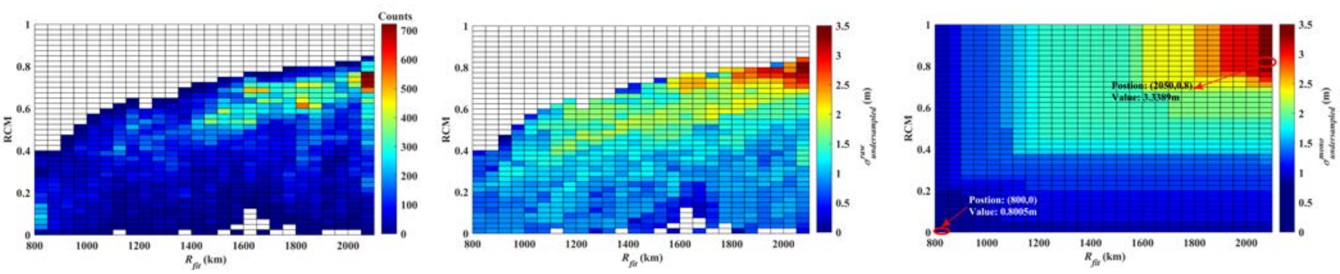

(a) (b) (c)

Fig. 5. Traditional $Rfit$-RCM geometry undersampled threat model
(a). Threat events distribution (b). Raw threat (c). Monotonic threat

Following the methodology described in the previous section, undersampled ionospheric threat samples were generated by treating individual IPPs as simulated IGPs and performing data deprivation at each candidate point. For each simulated IGP, surrounding observations were selected according to the predefined search strategy, and ionospheric delay estimation was carried out using the remaining samples after deprivation. Meanwhile, the corresponding geometric descriptors of the sampling configuration were recorded, together with the 90th percentile gradient derived from the observations used for estimation, so as to capture undersampled events as completely as possible under different ionospheric and sampling conditions. For the conventional model, the resulting undersampled events were parameterized only by the two geometric metrics, R_{fit} and RCM, and then organized into a two-dimensional threat space. The associated $\sigma_{undersampled}$ were grouped according to each bin, and the maximum value in each bin was selected to construct the raw threat model. For the proposed approach, ionospheric gradient information was further incorporated as an additional dimension, leading to a coupled geometry-gradient three-dimensional model defined by R_{fit}, RCM, and P90G.

As illustrated in Fig. 5(a), there are 69331 unique undersampled events in total detected during this storm period. The final RR-2D undersampled threat model, derived by applying monotonic logic to the raw model in Fig. 5(b), is presented in Fig. 5(c). During the monotonic bounding process, points at which the $\sigma_{undersampled}$ value remains unchanged are defined as critical points, as they represent the bounding values for their corresponding local regions in the threat space. For the conventional RR-2D model, the first critical point appears at R_{fit} = 800 km and RCM = 0. This indicates that the minimum undersampled threat in the model is 0.8005m rather than zero. Similarly, particular attention is given to the last critical point, which characterizes the upper bound of the threat space. This point represents the condition beyond which further increases in the geometric metrics no longer lead to higher $\sigma_{undersampled}$. In this case, the last critical point is located at R_{fit} = 2050 km and RCM = 0.8, corresponding to a maximum $\sigma_{undersampled}$ of 3.3389 m.

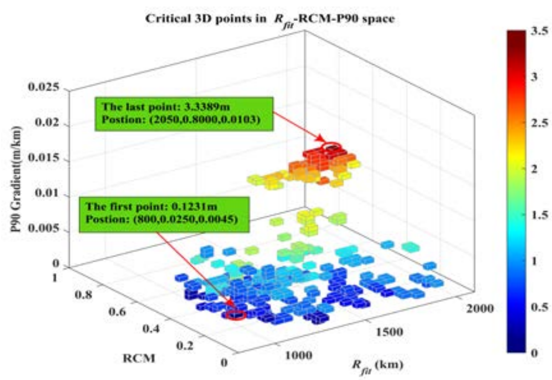

Fig. 6. Critical points of RRG-3D threat model

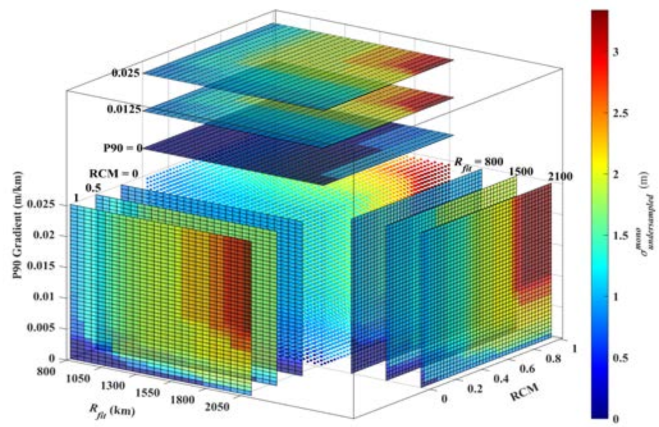

Fig. 7. Slice Visualization of the RRG-3D model

Due to the high dimensionality of the 3D undersampled threat model, direct visualization of the raw threat space is not straightforward. Therefore, Fig. 6 presents the distribution of all critical points in the R_{fit}-RCM-P90 gradient space, where the corresponding $\sigma_{undersampled}$ values are indicated by colour. Compared with Fig.5(c), which corresponds to the conventional RR-2D model, a key difference can be observed in the location of the first critical point. In the RRG-3D model, the first critical point does not appear in the first bin of the threat space. Instead, it is located at R_{fit} = 800 km, RCM = 0.0250, and P90G = 0.0045, with a corresponding $\sigma_{undersampled}$ of 0.1231 m. This value is significantly smaller than the minimum value observed in the RR-2D model. Moreover, this implies that when all three metrics are below the thresholds defined by this first critical point, the corresponding condition can be considered as not leading to an undersampled threat. The last critical point is identified at R_{fit} = 2050 km, RCM = 0.8, and P90G = 0.0103, corresponding to the maximum $\sigma_{undersampled}$ of 3.3389 m. While the maximum value remains consistent with that of the RR-2D model, the condition required to reach this maximum in the RRG-3D model is more restrictive. In addition to large geometric metrics, the gradient must also exceed the threshold of P90G (0.0103), indicating that extreme undersampled threats are jointly governed by both sampling geometry and ionospheric variability. To further illustrate the structure of the proposed model, Fig. 7 presents a multi-slice visualization of the geometry-gradient coupled undersampled threat space. The slices taken along different fixed dimensions clearly show how the inclusion of gradient refines the threat distribution. Compared with the RR-2D model, the RRG-3D model significantly reduces $\sigma_{undersampled}$ in regions with low gradient, while preserving strict bounding behaviour under high-gradient conditions.

Overall, these results demonstrate that the RRG-3D model effectively mitigates the over-conservatism of GIVE under low-gradient conditions, while providing a more stringent and physically meaningful definition of extreme undersampled threats.

B. Integrity Validation

Integrity validation in SBAS aims to ensure that the broadcast ionospheric uncertainty, expressed as GIVE, can conservatively bound the residual ionospheric delay error with a probability of 99.9%. To evaluate the integrity performance of the proposed method, this section adopts a two-fold validation framework. (1) At the GIVE level, GIVD estimation is first performed for all 117 BDSBAS IGPs using the available ionospheric observations during the selected period. Based on the estimated GIVDs, the undersampled threat is characterized using the conventional RR-2D model shown in Fig. 5(c) and the proposed RRG-3D model illustrated in Fig. 7. The corresponding $\sigma_{undersampled}$ is then derived and translated into GIVE values at each IGP, enabling a comparative assessment of the proposed ionospheric gradient modeling in reducing undersampled threats and mitigating excessive conservatism in GIVE. (2) Integrity is further validated by treating all IPPs as simulated IGPs, where the observed ionospheric delays are regarded as the ground truth. The normalized residual errors are computed using the corresponding GIVE values, and their statistical distribution is compared against the Gaussian overbounding threshold corresponding to a 99.9% probability. Integrity is considered to be satisfied when the normalized residuals are effectively bounded within this confidence level.

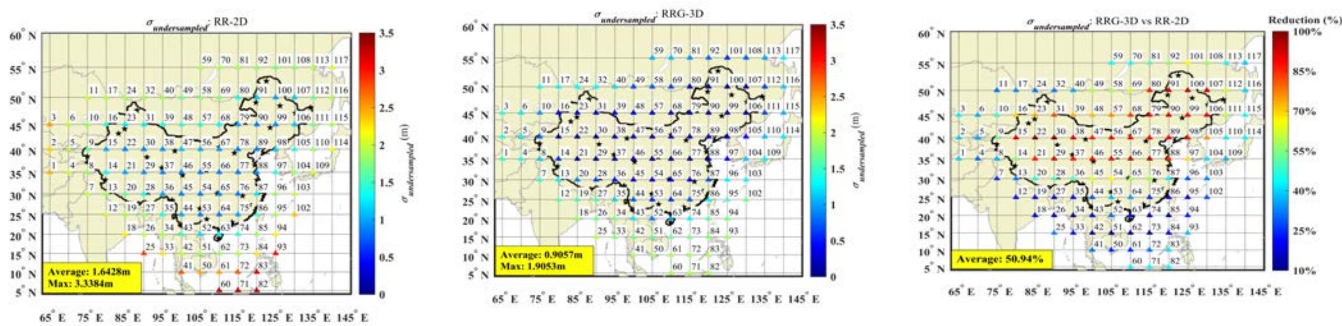

(a) (b) (c)

Fig. 8. Averaged undersampled threat results at 117 BDSBAS IGPs: (a) RR-2D model, (b) RRG-3D model, and (c) reduction in undersampled threats relative to the RR-2D model.

As shown in Fig. 8, the averaged undersampled threat results at 117 BDSBAS IGPs are presented for (a) the RR-2D model, (b) the RRG-3D model, and (c) the corresponding reduction relative to RR-2D. By comparing Fig. 8(a) and (b), it can be clearly observed that, compared with the conventional RR-2D model, the incorporation of ionospheric gradient information in the RRG-3D model significantly reduces the undersampled threats. Specifically, the maximum threat is reduced from 3.3384 m (IGP 82) to 1.9053 m (IGP 60), while the IGP-level averaged undersampled threat decreases from 1.6428 m to 0.9057 m, demonstrating a substantial overall mitigation effect. From Fig. 7(a), it is evident that the RR-2D model tends to produce larger undersampled threats at marginal IGPs, particularly in low-latitude regions below 20°N, where most values exceed 2.5 m. In contrast, the RRG-3D model effectively constrains these large threats to below 1.9053 m, indicating its capability in capturing spatial ionospheric variability and reducing overestimation caused by insufficient modelling of gradients. Further insights can be obtained from the reduction map in Fig. 7(c). Interestingly, the most significant reductions are observed at center IGPs, where ionospheric gradients are generally mild. In these regions, the reduction exceeds 70% for most IGPs, with a maximum reduction of 99.73% at IGP 22 (from 0.8781 m to 0.0024 m). Notably, both values are close to the minimum threat levels of the respective models, indicating that many locations previously inflated to non-negligible threats under the RR-2D model are effectively reclassified as negligible under the RRG-3D model. This highlights that the proposed method can substantially reduce unnecessary conservatism in regions with low ionospheric variability. In contrast, at marginal IGPs, the reduction is generally limited to 10%–40%, especially in low-latitude areas where strong local ionospheric gradients are more prevalent. This suggests that, although the RRG-3D model improves threat characterization, its effectiveness is inherently constrained in regions dominated by highly dynamic ionospheric behaviour.

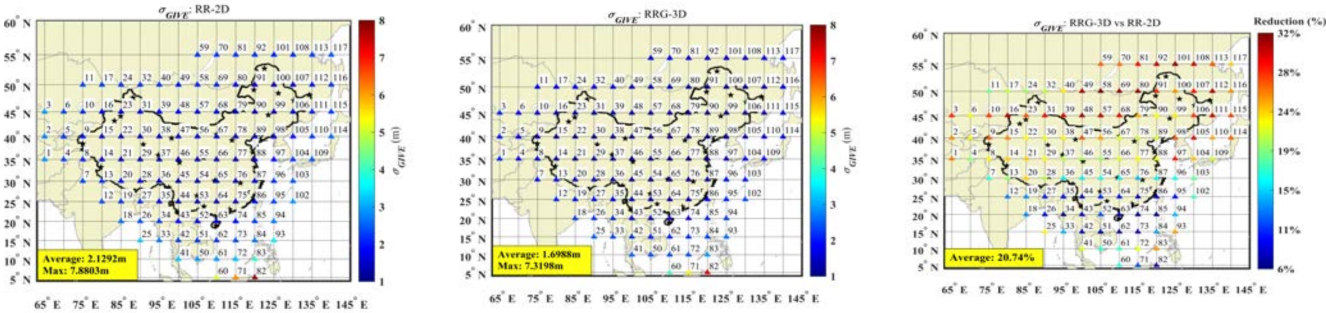

(a) (b) (c)

Fig. 9. Averaged total uncertainty results at 117 BDSBAS IGPs: (a) RR-2D model, (b) RRG-3D model, and (c) reduction in σ_{GIVE} relative to the RR-2D model.

Similarly, since the proposed RRG-3D model only modifies the characterization of the undersampled threat, the resulting total uncertainty (σ_{GIVE}) exhibits a consistent trend with that observed in the undersampled threats. As shown in Fig. 9(a) and (b), the lowest σ_{GIVE} values are generally observed at center IGPs, while the largest values occur at marginal IGPs, with the maximum consistently located at IGP 82 in the low-latitude region. This spatial pattern reflects the dominant influence of ionospheric variability, which is typically more pronounced at low latitudes and near the boundary of the monitoring network. Quantitatively, the proposed RRG-3D model achieves an average IGP-level reduction of 20.74% in σ_{GIVE}. The reduction is more significant at center IGPs and higher-latitude regions, where ionospheric gradients are relatively mild, with most reductions exceeding 20%. In contrast, at low-latitude marginal IGPs, the reduction is generally limited to below 15%, indicating that the effectiveness of the proposed method is constrained in regions characterized by strong and highly localized ionospheric gradients.

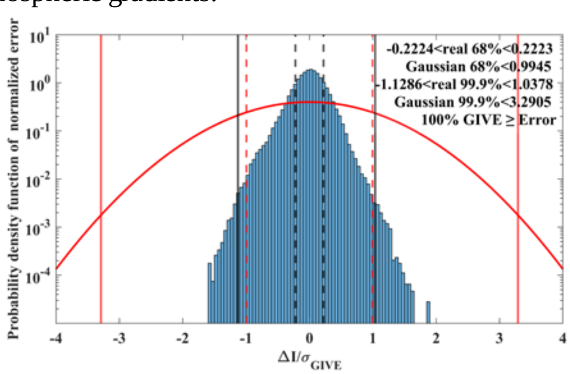

Fig. 10. Normalized error bound under storm conditions based on RR-2D model

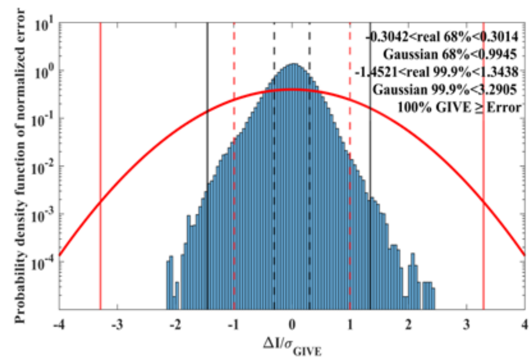

Fig. 11. Normalized error bound under storm conditions based on RRG-3D model

Following the approach proposed by Walter (Walter et al. 2001), the integrity of the gradient-aware undersampled ionospheric threat model is evaluated using the normalized ionospheric delay error. Under the selected storm conditions, all available IPPs within the study region are treated as simulated IGPs to provide a sufficiently large validation dataset. Based on the corresponding undersampled threat model (RR-2D or RRG-3D), the associated GIVE values are determined. The normalized error is defined as the difference between the observed and estimated ionospheric delays divided by σ_{GIVE}. The horizontal axis in Fig. 10 and Fig. 11 represents the normalized error $\Delta I/\sigma_{GIVE}$, while the vertical axis shows the empirical probability density function (PDF) in logarithmic scale. The histogram illustrates the empirical PDF, overlaid with the standard normal distribution, and the dashed and solid vertical lines indicate the 68% and 99.9% quantiles, respectively.

From the statistical results in Fig. 10 and Fig. 11, it can be observed that both the RR-2D and RRG-3D models fully satisfy the overbounding requirement, as the normalized residual errors are entirely bounded within the GIVE-derived limits in all cases. This confirms that both models meet the integrity requirement. However, under the same integrity constraint, the RRG-3D model exhibits a less conservative behaviour, significantly reducing the over-conservatism of the total uncertainty compared to the RR-2D model. Specifically, the 99.9% normalized error interval of the RRG-3D model is [-1.4521, 1.3438], compared to [-1.1286, 1.0378] for the RR-2D model, corresponding to an increase in interval width of 29.06%. Notably, this interval remains well within the standard Gaussian bound of 3.2905, indicating that the RRG-3D model can strictly satisfy the 99.9% integrity requirement of BDSBAS while effectively reducing the excessive conservatism inherent in the conventional geometry-based undersampled threat model.

C. Availability Simulation

A regional availability analysis is further conducted by replacing the broadcast ionospheric corrections with GIVDs estimated using the UnK method and GIVEs derived from the RR-2D and RRG-3D models and evaluating the resulting user protection levels across the service region. Availability performance is characterized in terms of HPL and VPL, which bound the horizontal and vertical position errors, respectively, with specified integrity probabilities. In this study, the 95% quantiles of HPL and VPL are adopted as availability indicators, where smaller protection levels correspond to higher availability. In this analysis, GPS satellite orbit and clock corrections were applied based on long-term and fast correction products from the CNES Navigation and Time Monitoring Facility (NTMF), while regional availability evaluation relied on augmentation information transmitted by the primary GEO satellite of BDSBAS (PRN 130). Users are uniformly distributed over a rectangular region.

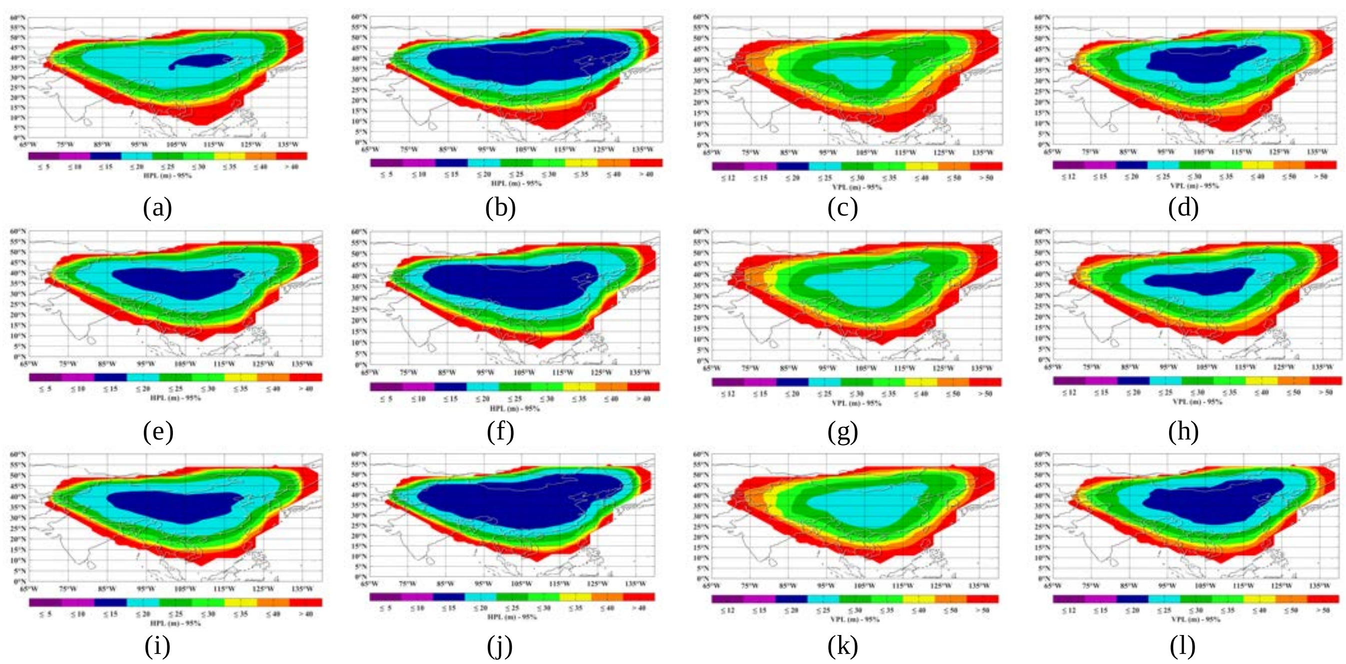

Fig. 12. Availability results of 95% PLs over China derived from the RR-2D and RRG-3D undersampled threat models over selected storm days. Each row corresponds to a specific day (from top to bottom: DOY 130, 132, and 133 of 2024), while each column shows, from left to right, HPL (RR-2D), HPL (RRG-3D), VPL (RR-2D), and VPL (RRG-3D).

As illustrated in Fig. 4, DOY 130 corresponds to the initial stage of the storm and represents relatively quiet ionospheric conditions, whereas DOY 132 and DOY 133 correspond to periods when the storm is actively developing. Accordingly, Fig. 12 presents the regional availability results for these three representative days. From Fig. 12, it can be observed that the effective coverage regions of RR-2D and RRG-3D are identical. This is because the GIVD estimation and IPP searching algorithm remain the same in both cases, and only the GIVE determination differs. Spatially, both HPL and VPL increase as the location moves away from the central region toward the boundaries, reflecting the degradation of geometric strength and ionospheric modelling capability at marginal areas.

Consistent with the GIVE performance analysis presented earlier, the RRG-3D model leads to a clear improvement in availability, which is directly reflected by the expansion of deep-blue regions corresponding to lower HPL and VPL values across all three days. This improvement is particularly evident over central regions, where ionospheric gradients are relatively mild and the reduction of over-conservative GIVE effectively translates into tighter protection levels. In contrast, the deep-red regions, which represent areas failing to meet the service requirements, are only marginally reduced under the RRG-3D model. This limitation is especially pronounced in low-latitude regions, where strong and highly localized ionospheric gradients dominate. As previously observed in the GIVE analysis, the performance gain of the RRG-3D model is constrained in such regions, resulting in limited availability improvement compared to central IGP areas.

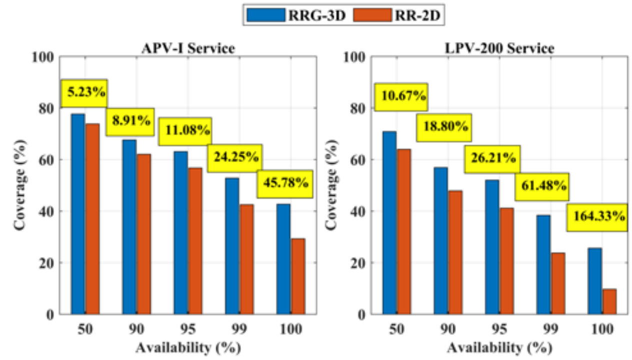

Fig. 13. Coverages with different availability levels based on RR-2D and RRG-3D for APV-I and LPV-200 services

The coverage performance over the study region is evaluated by comparing the resulting protection levels against the alert limits for different services, including APV-I (HAL = 40 m, VAL = 50 m) and LPV-200 (HAL = 40 m, VAL = 35 m). Fig. 13 presents the coverage results for both services at different availability levels, obtained as daily-averaged results over the selected storm days, while more detailed day-by-day statistics are provided in Table I.

Table I. Daily coverage results with different availability levels for APV-I and LPV-200 services (Left: RR-2D, Right: RRG-3D)

Coverage (%) on DOY	APV-I service					LPV-200 service				
	50%	90%	95%	99%	100%	50%	90%	95%	99%	100%
130	73.77 /77.94	61.03 /67.44	54.63 /61.92	34.45 /49.00	18.47 /39.22	63.88 /70.78	46.55 /56.76	37.12 /50.71	13.63 /31.92	2.28 /16.33
131	73.81 /78.08	62.31 /68.01	57.01 /63.20	43.10 /53.13	28.29 /42.28	63.95 /71.32	47.83 /57.86	41.85 /52.49	22.42 /39.25	4.80 /26.58
132	73.82 /76.14	61.89 /65.53	56.62 /61.04	41.20 /49.86	27.28 /37.86	63.92 /69.09	47.83 /54.10	41.45 /48.86	23.58 /33.01	6.70 /21.26
133	73.80 /78.36	62.43 /68.71	57.42 /64.79	46.21 /55.96	36.17 /48.59	63.94 /72.69	48.02 /58.99	42.08 /54.72	28.84 /44.04	19.26 /32.00
134	73.78 /78.05	62.24 /68.04	57.07 /63.20	42.93 /53.05	27.68 /41.54	64.02 /70.64	47.95 /57.00	41.65 /52.83	23.01 /40.01	4.24 /25.15
135	73.79 /77.39	62.43 /67.70	57.83 /64.17	47.01 /55.70	37.86 /47.72	64.14 /70.26	48.97 /56.52	42.91 /52.21	31.09/ 41.99	20.83 /32.26
Average	73.80 /77.66	62.04 /67.57	56.76 /63.05	42.48 /52.78	29.29 /42.70	63.97 /70.80	47.87 /56.87	41.18 /51.97	23.76 /38.37	9.68 /25.60

As illustrated, the proposed RRG-3D model consistently outperforms the conventional RR-2D model across all evaluated availability levels for both services. For the APV-I service, the RRG-3D model achieves coverage improvements of 5.23%, 8.91%, 11.08%, 24.25%, and 45.78% at availability levels of 50%, 90%, 95%, 99%, and 100%, respectively. A similar but more pronounced trend is observed for the LPV-200 service, where the coverage improvements are even greater, reaching 164.33% at 100% availability.

Moreover, it is evident that the coverage improvement becomes increasingly significant as the availability requirement becomes more stringent. This indicates that the proposed RRG-3D model is particularly effective in challenging scenarios requiring high availability, where the reduction of over-conservative GIVE plays a critical role in maintaining service continuity.

IV. Conclusions

This paper proposes a gradient aware undersampled ionospheric threat model with multiple metrics for BDSBAS, which extends the conventional geometry-based RR-2D framework by incorporating an additional ionospheric gradient descriptor into the threat characterization process. The proposed RRG-3D framework introduces the P90G metric to explicitly capture local ionospheric variability, addressing the limitation that spatial geometry alone cannot fully represent ionospheric irregularities. Using storm period data over the China region, the results demonstrate that the inclusion of gradient information enables a more physically meaningful representation of undersampled conditions. In particular, the proposed model effectively distinguishes between geometrically similar but physically different ionospheric scenarios, thereby improving the balance between conservatism and realism in undersampled threat modelling.

Extensive experimental results validate the effectiveness of the proposed RRG-3D model from both integrity and availability perspectives. At the IGP level, the incorporation of gradient information leads to a substantial reduction in undersampled threat, with the maximum value decreasing from 3.3384 m to 1.9053 m and the average value reduced from 1.6428 m to 0.9057 m. Correspondingly, the total uncertainty σ_{GIVE} is reduced by an average of 20.74%. Integrity validation based on normalized error analysis confirms that both RR-2D and RRG-3D satisfy the 99.9% overbounding requirement, while the proposed model significantly reduces excessive conservatism, as reflected by a 29.06% decrease in the 99.9% real data interval width. These improvements directly translate into enhanced regional availability. The results show that the RRG-3D model consistently reduces HPL and VPL values and expands the service coverage, with APV-I coverage improvements ranging from 5.23% to 45.78% under different availability levels and LPV-200 improvements reaching up to 164.33% under 100% level. The improvement is most pronounced in central regions with mild gradients, while the gain is relatively limited in low latitude marginal regions where strong ionospheric gradients dominate.

The contribution of this work is threefold. First, it demonstrates that ionospheric gradient is a critical physical factor that complements conventional geometry-based metrics in undersampled threat modelling. Second, it establishes a coupled geometry-gradient based three-dimensional threat model that effectively reduces excessive GIVE conservatism while strictly preserving integrity requirements. Third, it shows that improving the physical representation of undersampled threats leads to tangible gains in SBAS availability, particularly under high availability constraints. These findings provide a practical and extensible framework for enhancing BDSBAS performance. Future work will focus on adaptive gradient thresholding and model refinement in low latitude regions, as well as validation over broader network configurations and longer temporal spans.

Declarations

Ethics approval and consent to participate

Not applicable.

Availability of data and materials

The authors would like to thank IGS/WHU for providing the data and products and Crustal Movement Observation Network of China (CMONOC) for providing GNSS observation data, and Crustal Dynamics Data Information System (CDDIS) for the supported provided with precise orbit products and ionospheric-related GNSS auxiliary data, and also like to thank the France National Center for Space Studies (CNES), Navigation and Time Monitoring Facility (NTMF) for WAAS messages.

Competing interests

The authors declare no conflict of interest.

Funding

The work described in this paper is supported by a grant from the Research Grants Council of the Hong Kong Special Administrative Region, China (15214523).

Authors' contributions

Hui Ren conceived the presented idea and developed the theory and analytical methods. Zhengzhen Jin contributed to manuscript formatting and proofreading. Tong Liu and Fangxin Hu provided and processed the CMONOC observation data. Yiping Jiang verified the data quality, provided critical feedback on the analytical methods, and supervised the findings of this work. All authors discussed the results and contributed to the final manuscript.

Acknowledgements

This research is funded by a grant from the

Research Grants Council of the Hong Kong Special Administrative Region, China (15214523). These supports are gratefully acknowledged.

Reference

[2]. Alleau P, Buscarlet G, Trilles S, Bossche M, Bigot J (2013) Comparative ionosphere electron content estimation method in SBAS performances. In: Proceedings of the 26th International Technical Meeting of the Satellite Division of The Institute of Navigation (ION GNSS+ 2013). pp 2523–2532

[3]. Altshuler ES, Fries RM, Sparks L (2001) The WAAS Ionospheric Spatial Threat Model. Proceedings of the 14th International Technical Meeting of the Satellite Division of The Institute of Navigation (ION GPS 2001) :2463–2467

[4]. Bang E, Lee J (2023) Undersampled Ionospheric Irregularity Threat Parameterization Using a Three-Dimensional Model for Satellite-Based Augmentation Systems. IEEE Transactions on Aerospace and Electronic Systems 59(2):1183–1201.

[5]. Bang E, Lee J, Seo J, Walter T (2013) Constructing ionospheric irregularity threat model for Korean SBAS. In: Proceedings of the ION 2013 Pacific PNT Meeting. pp 296–306

[6]. Blanch J, Walter T, Enge P (2018) Gaussian bounds of sample distributions for integrity analysis. IEEE Transactions on Aerospace and Electronic Systems 55(4):1806–1815

[7]. Blanch J, Walter T, Enge P (2002) Ionospheric Threat Model Methodology for WAAS. Navigation 49(2):103–107.

[8]. Datta-Barua S (2004) Ionospheric Threats to Space-Based Augmentation System Development. pp 1308–1317

[9]. El-Arini MB, Conker RS, Albertson TW, Reagan JK, Klobuchar JA, Doherty PH (1994) Comparison of Real-Time Ionospheric Algorithms for a GPS Wide-Area Augmentation System (WAAS)*. Navigation 41(4):393–414.

[10]. Jiang Y, Wang J (2016) A New Approach to Calculate the Horizontal Protection Level. J Navigation 69(1):57–74.

[11]. Junjie B, Rui L, Pan L, Zhigang H (2018) Impact of ionospheric irregularity on SBAS integrity: Spatial threat modeling and improvement. Journal of Systems Engineering and Electronics 29(5):908–917.

[12]. Lee J, Yoon M, Pullen S, Gillespie J, Mather N, Cole R, de Souza JR, Doherty P, Pradipta R (2015) Preliminary Results from Ionospheric Threat Model Development to Support GBAS Operations in the Brazilian Region. pp 1500–1506

[13]. Li W, Jiang Y (2023) Seasonality of Nominal Ionospheric Gradient Using Time-Step Method Based on GNSS CORS Observations in Hong Kong. Denver, Colorado, pp 531–537

[14]. Liu D, Yu X, Chen L, Zhen W (2017) Analysis on Ionospheric Delay Variogram Modeling in China. In: Sun J, Liu J, Yang Y, Fan S, Yu W (eds) China Satellite Navigation Conference (CSNC) 2017 Proceedings: Volume II. Springer, Singapore, pp 119–130

[15]. Marini-Pereira L, Pullen SP, de Oliveira Moraes A (2021) Reexamining Low-Latitude Ionospheric Error Bounds: An SBAS Approach for Brazil. IEEE Transactions on Aerospace and Electronic Systems 57(1):674–689.

[16]. Pandya N, Gran M, Paredes E (2007) WAAS Performance Improvement with a New Undersampled Ionospheric Gradient Threat Model Metric. San Diego.

[17]. Prasad N, Sarma AD (2007) Preliminary analysis of grid ionospheric vertical error for GAGAN. GPS Solut 11(4):281–288.

[18]. Ren H, Jiang Y, Liu T (2024) An Anisotropic Kriging for Ionospheric Delay Interpolation With a Wide Area Reference Network. IEEE Transactions on Geoscience and Remote Sensing 62:1–13.

[19]. Saito S, Nakamura M, Yoshihara T, Le Huy M, Nguyen Chien T, Supriadi S, Abadi P, Unggul Prabowo D (2025) Characterizing ionospheric delay gradients for GNSS ground-based augmentation system. In: Lin C-T, Tseng T-P, Lin C-H, Yang S-C (eds) Advancement on GNSS-based Measurements and Applications. SPIE, Kaohsiung, Taiwan, p 9

[20]. Saito S, Yoshihara T (2017) Evaluation of extreme ionospheric total electron content gradient associated with plasma bubbles for GNSS Ground-Based Augmentation System. Radio Science 52(8):951–962.

[21]. Sakai T, Matsunaga K, Hoshinoo K, Walter T (2008) Modeling Ionospheric Spatial Threat Based

on Dense Observation Datasets for MSAS.
[22]. Sparks L, Blanch J, Pandya N (2011) Estimating ionospheric delay using kriging: 1. Methodology. Radio Science 46(06):1–13
[23]. Trilles S, Authié T, Renaze C, Raoul O (2015) Robust EGNOS availability performances under severe ionospheric conditions. In: Proceedings of the 28th International Technical Meeting of the Satellite Division of The Institute of Navigation (ION GNSS+ 2015). pp 1783–1789
[24]. Walter T, Hansen A, Blanch J, Enge P, Mannucci T, Pi X, Sparks L, Iijima B, El-Arini B, Lejeune R, Hagen M, Altshuler E, Fries R, Chu A (2001) Robust Detection of Ionospheric Irregularities. Navigation 48(2):89–100.
[25]. Wang H, Fang K, Wang Z, Lan X, Hou X, Zhu Y (2025) Optimizing Ionospheric Semi-variograms with Variable Correlation Parameters and Modeling Spatial Threats with Multiple Metrics for China Region. IEEE Trans Aerosp Electron Syst :1–22.
[26]. Wang Z, Wang S, Zhu Y, Xin P (2017) Assessment of Ionospheric Gradient Impacts on Ground-Based Augmentation System (GBAS) Data in Guangdong Province, China. Sensors 17(10):2313.
[27]. Zhang Q, Li R, Wang Z (2017) An Improved Ionospheric Spatial Threat Model for SBAS. Chinese Journal of Electronics 26(5):1105–1110.
[28]. Zhang Y, Xiao Z, Liu Z, Tang X, Ou G (2020) SBAS performance improvement with a new undersampled ionosphere threat model based on relative coverage metric. Journal of Atmospheric and Solar-Terrestrial Physics 198:105178.

Authors

Hui Ren received the master's degree in mechanical engineering from the Hong Kong University of Science and Technology, Hong Kong, China, in 2022. He is currently pursuing a Ph.D. degree at The Hong Kong Polytechnic University. His research interests include ionospheric modeling and satellite-based augmentation systems (SBAS) integrity monitoring.

Zhengzhen Jin received the B.S. from the School of Integrated Circuit Science and Engineering, Tianjin University of Technology, Tianjin, China in 2025. He is pursuing a master's degree at The Hong Kong Polytechnic University. His main research interests include the satellite navigation, integrated Navigation and integrated circuit design

Tong Liu received his bachelor's and master's degrees from Shandong University and later obtained his doctoral degree from Harbin Institute of Technology (Shenzhen). He is currently a postdoc fellow within the Research Talent Hub in Hong Kong. His research is focused on space weather and geodesy, with a particular interest in ionospheric effects on GNSS, including the observation, impact, modelling, and mitigation strategies.

Fangxin Hu obtained his B.E. and M.E. degrees in School of Geodesy and Geomatics of Wuhan University, China, in 2021 and 2024. He is now pursuing the Ph.D. degree at the School of Aerospace, Harbin Institute of Technology (Shenzhen), China. His current research interests are Global Navigation Satellite System (GNSS) meteorology, high-precision GNSS data processing and deep learning in meteorology.

Yiping Jiang obtained her Ph.D degree from the university of new south wales, Sydney, Australia in 2014.
She is an assistant professor at the department of aeronautical and aviation engineering, the Hong Kong Polytechnic University. Her research interests include precise positioning and integrity monitoring for civil aviation and intelligent transportation systems. Currently, she lectures on avionics systems and satellite navigation for undergraduate and postgraduate students.